Spin caloritronics in two-dimensional CrI$_3$/NiCl$_2$ van der Waals heterostructures

Xingyi Tan,[1] Linjie Ding,[1] Gui-Fang Du,[2] and Hua-Hua Fu[2,*]

[1]*Department of Physics, Chongqing Three Gorges University, Wanzhou 404100, China*

[2]*School of Physics and Wuhan National High Magnetic Field Center, Huazhong University of Science and Technology, Wuhan 430074, China*

Two-dimensional van der Waals (vdW) heterostructures have recently emerged as attractive candidates to work as spintronic and optoelectronic devices. Here, two types of magnetic CrI$_3$/NiCl$_2$ vdW heterostructures are constructed to design spin caloritronic devices. The first-principles calculations uncover that the magnetic configurations of CrI$_3$/NiCl$_2$ vdW heterostructures can be converted easily to a ferromagnetic, an antiferromagnetic, and even a bipolar magnetic semiconducting state by an external electric field. More interestingly, two thermal spin-dependent currents with opposite spin orientations can be driven by a temperature gradient to flow in opposite transport directions independently in the different layers of vdW heterostructures, demonstrating that the CrI$_3$/NiCl$_2$ vdW heterostructures can exhibit a nearly perfect thermal spin-filtering effect in each layer while generating a well-defined spin-Seebeck effect in the whole system. Our work puts forward a class of material candidates to design spin caloritronic devices characterized by multiple inspiring thermal-spin transport behaviors.

I. INTRODUCTION

Spin caloritronics, combining two independent research fields of thermoelectrics and spintronics, has attracted an enormous amount of attention due to its promising device applications and underlying fundamental science [1–9]. One of the core topics in this field is the spin-Seebeck effect (SSE), which focuses on how to generate a spin current by a temperature gradient in magnetic materials. This effect was first discovered experimentally in magnetic metals [1], and then observed in ferromagnetic (FM) metals/semiconductors/insulators [10,11], antiferromagnetic (AFM) [12], paramagnetic [13], and even nonmagnetic (NM) materials [14]. To push spin caloritronics toward practical device applications, a typical kind of SSE, i.e., a conduction electron-based SSE, has been proposed in a series of realistic material candidates such as graphene [15–17], silicene [18], and phosphene [19] nanoribbons [12,13,18,20–22], in which the spin-dependent currents with opposite spin orientations are driven to flow in opposite directions by a temperature gradient. However, two spin-dependent transport channels for thermal spin currents are usually localized at the edges of the same FM nanoribbons [23]. Thus, limited by the spatial symmetry of two spin transport channels, it is very difficult to manipulate any one of the spin-dependent currents independently. Meanwhile, the spatial separations of two spin channels in FM nanoribbons reduce the overlap of two charge currents with opposite transport directions, which is not beneficial to generate a pure spin current by reducing the accumulation of charge carriers [24]. These drawbacks inspire us to explore new material structures to realize the SSE together with the controllable thermal spin currents.

We are well aware that two-dimensional (2D) materials based on van der Waals (vdW) heterostructures have long been regarded as promising candidates to design spintronic and optoelectronic devices, due to their high carrier mobility, broad energy spectra, and tunable electronic structures [25–30]. However, realization of the SSE and other exotic thermal-spin effects in vdW heterostructures has been rarely reported so far. If we push the vdW heterostructures toward spin caloritronic device applications, one of the key features, i.e., the FM semiconducting, should appear in them [31–34]. It is regrettable that up to now, only a very small number of FM vdW semiconducting heterostructures have been demonstrated. For example, both a FM ground state and high Curie temperature (T_C) have been proposed in Mg(OH)$_2$/VS$_2$ bilayer with vdW-type interactions [35]. Moreover, a FM semiconducting property characterized by a high T_C has been observed in the 2D transition-metal dichalcogenide-based vdW heterostructures (MoS$_2$/VS$_2$ and WS$_2$/VS$_2$) [36], although the FM state originates only from one layer (i.e., the VS$_2$ layer). It should be stressed that to obtain a well-defined SSE with controllable spin-dependent currents in vdW heterostructures, the FM semiconducting feature should be required in every layer, which also drives us to explore unique while feasible 2D vdW heterostructures.

In this work, we propose two types of CrI$_3$/NiCl$_2$ vdW heterostructures with stable magnetic configurations. The first-principles calculations show that both of their layers display the FM semiconducting feature, while the whole system shows an AFM ground state. More interestingly, by applying an external electric field, the magnetic CrI$_3$/NiCl$_2$ vdW heterostructures exhibit a bipolar magnetic semiconducting (BMS) state. The unique spin-splitting electronic structures determine that every layer of the vdW heterostructures provides a spin-dependent transport channel, i.e., one layer for spin-up electrons and the other for spin-down ones.

---

*Author to whom all correspondence should be addressed: hhfu@mail.hust.edu.cn

Then, we construct a spin caloritronic device based on the one type of $CrI_3/NiCl_2$ vdW heterostructures and thermally driven spin-dependent currents, which are calculated from the density-functional theory (DFT) combined with the nonequilibrium Green's function (NEGF) approach. We show that the spin-up and spin-down currents flow independently in the different layers with opposite flow directions, indicating that every layer of the $CrI_3/NiCl_2$ vdW heterostructure exhibits a nearly perfect thermal spin-filtering effect (SFE) with the spin polarization as high as 100%, while the whole device exhibits a well-defined SSE, contributing to generate a pure thermal spin current or a thermoelectric spin voltage. Our theoretical results not only put forward realistic material structures to realize the SSE combined with the SFE, but they also push spin caloritronics toward practical device applications with multiple exotic thermal-spin effects.

The remainder of this paper is organized as follows. In Sec. II, two models of the $CrI_3/NiCl_2$ vdW heterostructure are constructed, and the theoretical methods to study their magnetic properties and to calculate thermal spin-dependent currents are introduced. In Sec. III, the numerical results, including the magnetic configurations and the modifications of spin-splitting bands by an external electric field, are discussed in detail, and then a spin caloritronic device based on the $CrI_3/NiCl_2$ vdW heterostructure is proposed. In addition, some thermal-spin effects, including SSE and SFE, are obtained, and their underlying physical mechanisms are analyzed in detail. The main results are summarized in the final section.

II. STRUCTURAL MODELS AND COMPUTATIONAL METHODS

The geometrical structures of $CrI_3/NiCl_2$ vdW heterostructures are illustrated in Fig. 1, where two possible stacking configurations of CrI_3 and $NiCl_2$ monolayers from structural optimization calculations are drawn. For Model A, one Cr atom sits on one Cl atom, and the other Cr atom sits on the Ni atom in a united cell, while for Model B, two Cr atoms sit on two Cl atoms. To get the structurally optimized vdW heterostructures, we perform the DFT combined with the NEGF method, which are integrated in the QUANTUM ATK package [37,38]. In our calculations, the generalized gradient approximation (GGA) of Perdew, Burke, and Ernzerhof (GGA-PBE) is selected for the electronic exchange and correlation [39,40]. In addition, the DFT-D_3 method of Grimme [41] is used to correct the vdW interactions in the heterostructures. Norm-conserving pseudopotentials are used [42], a cutoff energy of 100 Hartree and the Monkhorst-pack $9 \times 9 \times 1$ k grid are selected for the electronic structure calculations, and a $1 \times 1 \times 100$ k-point grid is used for the transport calculations. Geometrical structures are relaxed until the forces and energy converge to 0.01 eV/Å and 10^{-5} eV. Considering that the $3d$ states of Cr and Ni atoms have a significant influence on the electronic structures of heterostructures, the Coulomb correlation **U** is considered in these two kinds of atoms, indicating that the GGA + **U** method is used in our first-principles calculations to ensure numerical accuracy [43]. According to previous reports [44–46], the effective **U** value in Cr atoms is adopted as $\mathbf{U}_{eff} = 2.65$ eV, and that in Ni atoms
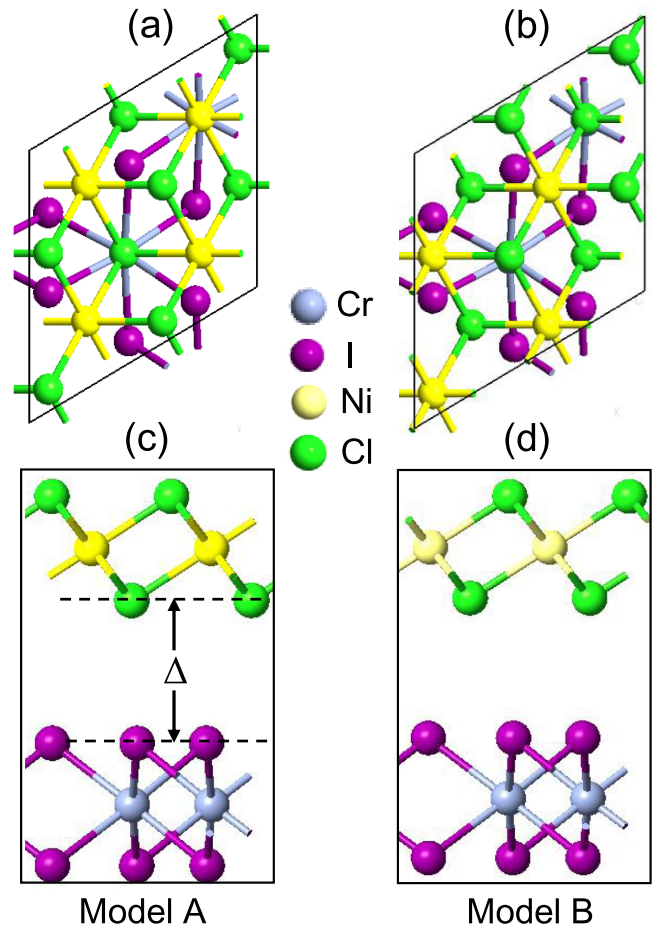

FIG. 1. Schematic structures of two typical models of $CrI_3/NiCl_2$ vdW heterostructures, i.e., Model A in (a) and (c), and Model B in (b) and (d). The upper parts from the top view and the lower parts from the side view. Ni, Cl, Cr, and I atoms are represented by the balls with different colors.

is $\mathbf{U}_{eff} = 3.0$ eV. Moreover, to gain comparable studies, the numerical results of $CrI_3/NiCl_2$ vdW heterostructures without considering **U** are also presented. Additionally, a vacuum region of 30 Å along the direction perpendicular to the layers is adopted for screening the interactions between two neighboring vdW heterostructures.

The numerical results show that both the CrI_3 and $NiCl_2$ monolayers host hexagonal lattice symmetry with the optimized lattice constant $a_1 = 6.877$ Å and $a_2 = 3.496$ Å, respectively, which are in good agreement with previous experimental data on bulk structures of the values 6.867 Å [47,48] and 3.488 Å [49], indicating that both calculation methods are reliable and the optimized parameters are reasonable. To decrease the mismatch, the vdW heterostructures are built on a CrI_3 unit cell and a $2 \times 2 \times 1$ $NiCl_2$ supercell. The lattice mismatch between CrI_3 and $NiCl_2$ is determined by the relation $\eta = 2(2a_2 - a_1)/(a_1 + 2a_2) \times 100\%$, which shows that there is a slight mismatch of 1.66% occurring in the vdW heterostructures, ensuring their structural stabilities. It is noted that the strain effect induced by lattice mismatch is not considered here, since some previous works also demonstrated that as the lattice strain is as high as

1.66% in the CrI_3 and $NiCl_2$ monolayers, almost no significant changes are observed in their electronic structures [50,51]. Then, to testify to the stability of the different patterns, we calculated their binding energies, which are defined as $E_h = (E_{CrI_3/NiCl_2} - E_{CrI_3} - E_{NiCl_2})/N$, where $E_{CrI_3/NiCl_2}$, E_{CrI_3}, and E_{NiCl_2} are the total energies of $CrI_3/NiCl_2$ vdW heterostructure, CrI_3 monolayer, and $NiCl_2$ monolayer, respectively, and N denotes the number of atoms of the $CrI_3/NiCl_2$ vdW heterostructure. The binding energies for Model A and Model B are -169.97 and -169.63 meV, implying that these two $CrI_3/NiCl_2$ stacking patterns are energetically stable. In addition, the binding energies for both models are nearly equal, indicating that Model A is located in the ground state while Model B is in the metastable state. Thus, in our studies we focus mainly on Model A, considering Coulomb correlation **U** both in Ni and Cr atoms, and we put the numerical results of Model A without **U** and Model B with (without) **U** in the Supplemental Material [52]. Nevertheless, we believe that both vdW heterostructures can be prepared in experiments, since 2H-$MoTe_2$ and 1T-$MoTe_2$ have already been fabricated successfully, although their binding energies are also different [53–60]. Additionally, the layer equilibrium distance, i.e., Δ drawn in Fig. 1(c), is 3.636 Å in Model A and 3.635 Å in Model B, supporting their same preparation possibilities.

III. RESULTS AND DISCUSSION

A. Magnetic configurations of the $CrI_3/NiCl_2$ vdW heterostructure

First, we should demonstrate the magnetic configurations of the $CrI_3/NiCl_2$ vdW heterostructure. To that end, we consider the total energies of three different magnetic phases, i.e., FM, AFM, and NM states in the system. It is noted that some previous studies uncovered that both 1T-$NiCl_2$ and CrI_3 monolayers host FM ground states [61,62]. Therefore, only the AFM configuration between the CrI_3 and $NiCl_2$ monolayers is considered here. Numerical results show that the energy difference $\Delta E_{AF} = E_{FM} - E_{AFM}$ and $\Delta E_{AN} = E_{NM} - E_{AFM}$, where E_{FM}, E_{AFM}, and E_{NM}, standing for the total energies of FM, AFM, and NM states, are 1.25 meV and 5.56 eV for Model A, confirming the AFM ground state in the $CrI_3/NiCl_2$ vdW heterostructure, which is similar to the CrS_2 bilayers [63]. Moreover, the total energies of the AFM and FM states are nearly equal, indicating that the $CrI_3/NiCl_2$ vdW heterostructure can be easily turned to the FM state under a small magnetic field [64–66]. These unique magnetic properties support their potential for spintronic device applications.

To understand the underlying mechanism of unique magnetic configurations of the $CrI_3/NiCl_2$ vdW heterostructure, we examine the band structures and spin alignments of isolated CrI_3, $NiCl_2$ monolayers, and the vdW-coupled $CrI_3/NiCl_2$ bilayer. For a CrI_3 monolayer, the conduction-band minimum (CBM) lies in the Γ-K line, while the valence-band maximum (VBM) is located at the Γ point, indicating that the CrI_3 monolayer has an indirect band gap of 1.17 eV with **U** (1.24 eV without **U**), as shown in Figs. S1(a) and S1(b) in the Supplemental Material [52]. For a $NiCl_2$ monolayer, the CBM lies along the Γ-M direction and the VBM is located at the Γ point, indicating that the $NiCl_2$ monolayer has an indirect band gap of 2.52 eV

with **U** [1.20 eV without **U**, as illustrated in Figs. S1(c) and S2(d) in the Supplemental Material [52]], which is in good agreement with the previous report [67]. For the $CrI_3/NiCl_2$ vdW heterostructure, the first-principles calculations show that the corresponding CBM lies in the Γ-M direction, and the VBM is located at the Γ point, indicating an indirect band gap of 0.91 eV, as shown in Fig. 2(a). Moreover, the CBM and VBM are contributed mainly by the $NiCl_2$ and CrI_3 layer, respectively. Therefore, type-II band alignments are formed in the $CrI_3/NiCl_2$ vdW heterostructure [68]. More interestingly, the CBM is composed of the spin-down states, while the VBM is composed of the spin-up ones, causing the $CrI_3/NiCl_2$ vdW heterostructure to exhibit a typical BMS feature [69–73]. As a result, the spin-down electrons may easily transfer from the CBM of the CrI_3 to the $NiCl_2$ layer, whereas the spin-polarized holes can transfer from the $NiCl_2$ to the CrI_3 layer. Additionally, the charge density (CD) difference $\Delta\rho$ ($=\rho_{hetero} - \rho_{CrI_3} - \rho_{NiCl_2}$) can be applied to understand the interaction between CrI_3 and $NiCl_2$ monolayers, where ρ_{hetero}, ρ_{CrI_3}, and ρ_{NiCl_2} denote the CDs of the heterostructure and the CrI_3 and $NiCl_2$ monolayer, respectively. As illustrated in Fig. 2(b), the navy blue and aubergine represent the electron depletion and accumulation, respectively. One can find that tunneling electrons are depleted mainly in the $NiCl_2$ layer while they accumulate in the CrI_3 layer.

Furthermore, it is established that the controllable spin-splitting band alignments are one of the key requirements to ensure a FM semiconducting heterostructure toward realistic spintronic device applications. Then, we examine the spin-dependent band alignments in the $CrI_3/NiCl_2$ vdW heterostructure. As illustrated in Fig. 2(c), the CBM and VBM of the $NiCl_2$ layer are obviously lower than those of the CrI_3 layer, confirming the typical characteristics of type-II band alignments in the system [68]. Moreover, we find that the spin-down bands have the typical characteristics of the type-II heterostructure, while the spin-up bands tend to display the typical characteristics of the type-I heterostructure [68]. Interestingly, the CB offsets (ΔE_C, 3.17 and 1.61 eV) and the VB offsets (ΔE_V, 1.65 and 1.91 eV) are observed for the spin-up and spin-down channels, respectively. Therefore, the different separation possibility of electrons and holes in the spin-up and spin-down channels also supports that the $CrI_3/NiCl_2$ vdW heterostructures have a great potential to serve as good-performance spintronic devices, due to effective spin-dependent manipulations.

B. Modifications of spin-splitting bands by an external electric field

From an experimental point of view, the gate-voltage modulation is an effective way to adjust the carriers' energy level relative to the Fermi level [35,36,74,75]. Now, we continue to examine the spin-splitting band engineering of the $CrI_3/NiCl_2$ vdW heterostructure by an external electric field. For convenience, the positive direction of the electric field is defined from the $NiCl_2$ to the CrI_3 layer. In Fig. 3, we plotted the band structures of the $CrI_3/NiCl_2$ vdW heterostructure as the external electric field E is changed from -0.8 to 0.8 V/Å in steps of 0.1 V/Å, and in Fig. 4 we presented the corresponding ΔE_{AF} and band gaps versus the strength
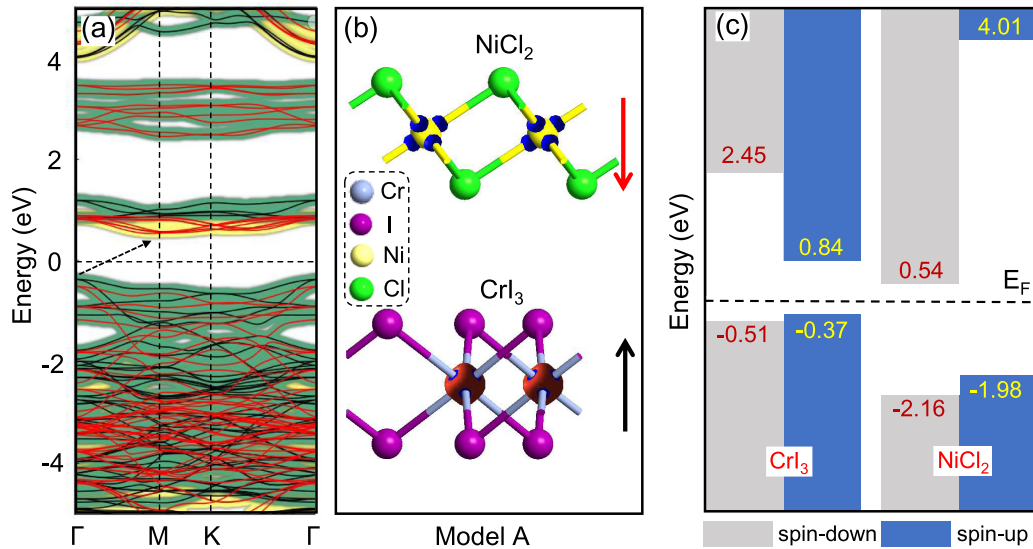
FIG. 2. (a) Band structures of $CrI_3/NiCl_2$ vdW heterostructure for Model A considering Coulomb correlation **U** both in Ni and Cr atoms, where the black (red) lines indicate the spin-up (-down) bands, and the light green (yellow) lines represent CrI_3 ($NiCl_2$). (b) Structural guidance for $CrI_3/NiCl_2$ vdW heterostructure with charge difference in an isosurface value of 0.005 $e/Å^3$ from the inside view. (c) The energy band offsets of the $CrI_3/NiCl_2$ vdW heterostructure, where the light gray and the blue stand for the spin-down and spin-up bands, respectively. The numbers in every column denote the band energies corresponding to the conduction-band minimum and the valence-band maximum.

of the external electric field. Obviously, the vdW heterostructure displays the FM ground state because $\Delta E_{AF} < 0$ and $\Delta E_{AN} > 0$ in the range $[-0.8, -0.2]$ V/Å of the electric field,

as illustrated in Fig. 4(a), while the AFM ground state is in the range $[-0.1, 0.8]$ V/Å, since $\Delta E_{AF} > 0$ and $\Delta E_{AN} > 0$. Similar results are also found in the CrI_3 bilayer [74]. What
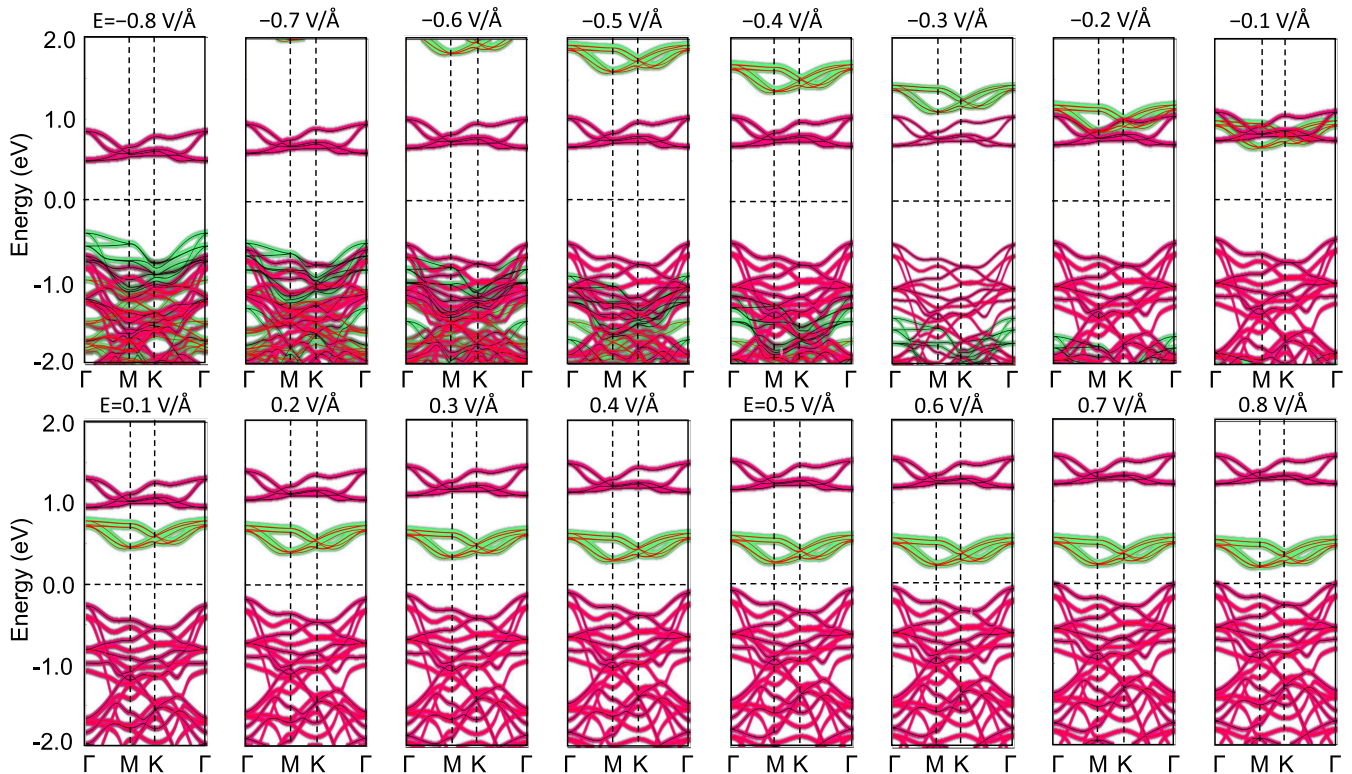

FIG. 3. Band structures of the $CrI_3/NiCl_2$ vdW heterostructure for Model A considering Coulomb correlation **U** under different external electric field (E) with a step of 0.1 V/Å. The upper levels from left to right are -0.8 to -0.1 V/Å, and the lower levels from left to right are 0.1–0.8 V/Å. The black line indicates spin-up bands and the red line indicates spin-down bands. The light green lines represent the $NiCl_2$, while the pink lines represent CrI_3.
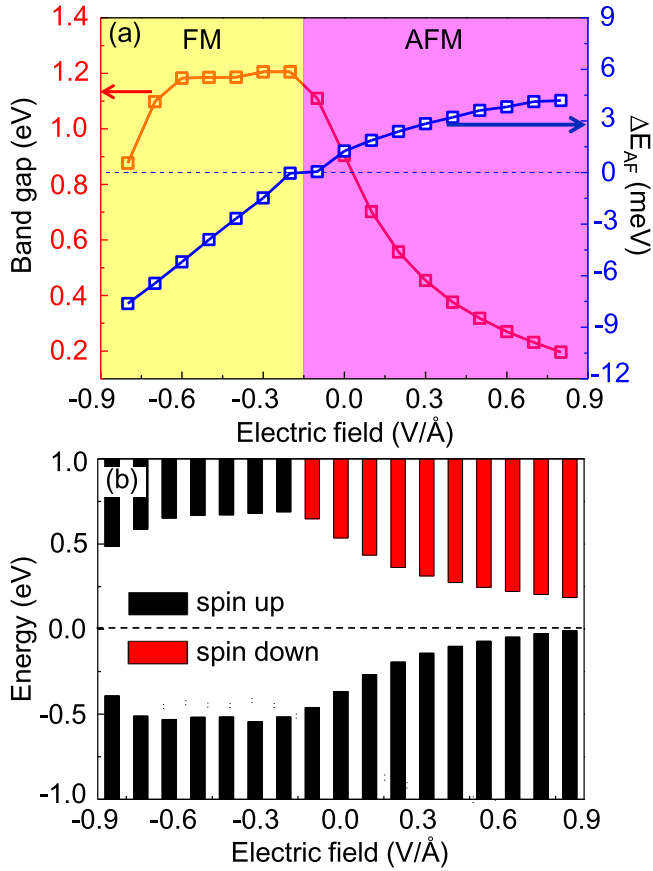
FIG. 4. (a) The band gap and ΔE_{AF} as a function of the strength of external electric field E in the $CrI_3/NiCl_2$ vdW heterostructure with Coulomb correlation **U** both in Cr and Ni atoms. (b) The band-gap edge as a function of the strength of external electric field E in the $CrI_3/NiCl_2$ vdW heterostructure.
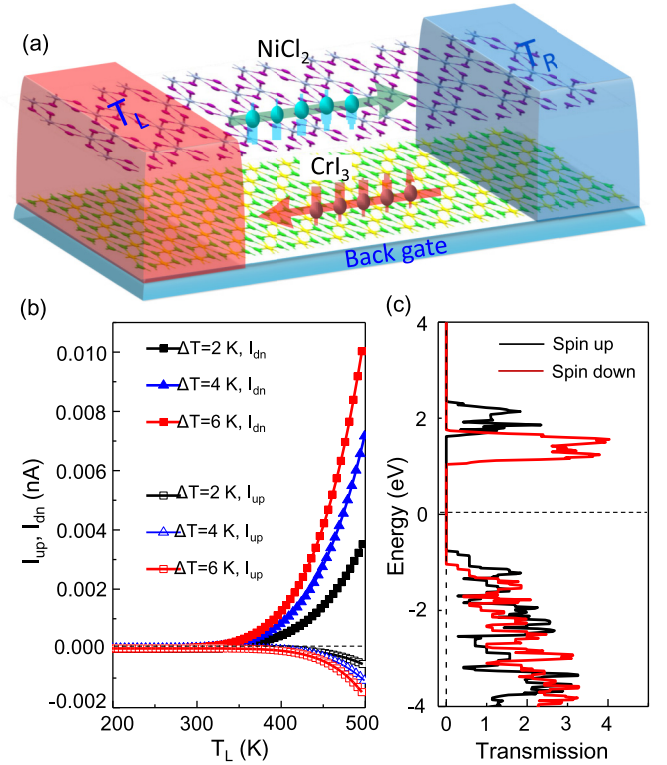

FIG. 5. (a) Schematic illustration of the spin caloritronic device based on the $CrI_3/NiCl_2$ vdW heterostructure with Coulomb correlation **U** both in Ni and Cr atoms. The spin-dependent currents are induced by $\Delta T = T_L - T_R$. (b) Thermally driven spin-up current I_{up} and spin-down current I_{dn} as a function of device temperature T_L in the device. (c) The spin-dependent transmission spectra of Model A, where the black lines denote spin-up electrons and the red lines denote spin-down electrons.

is more, ΔE_{AF} is near zero, indicating that the FM state is a metastable state in the range $[-0.1, 0.8]$ V/Å. Thus, the vdW heterostructure can be easily converted to the FM state in this range under a small magnetic field [64–66], confirming further its potential spintronic device applications.

It is clearly seen that the band gap of the $CrI_3/NiCl_2$ vdW heterostructure is sensitive to the external electric field, i.e., the band gap decreases monotonically with an increasing electric field in the range $[-0.3, 0.8]$ V/Å, while it increases in the range $[-0.8, -0.3]$ V/Å. These asymmetric variations imply that the electronic properties in the $CrI_3/NiCl_2$ vdW heterostructure are highly dependent on the external electric field, which is very similar to that of the $Mg(OH)_2/VS_2$ heterostructure [35]. Moreover, in the range $[-0.8, -0.2]$ V/Å, both the CBM and the VBM are contributed by spin-up bands, indicating that the vdW heterostructure displays a magnetic semiconducting behavior, as shown in Fig. 4(b). Meanwhile, both the VBM and the CBM are located at the Γ point, as shown in Fig. 3, indicating that the $CrI_3/NiCl_2$ vdW heterostructure is a typical direct-band-gap magnetic semiconductor. Furthermore, both the CBM and the VBM are contributed mainly by the CrI_3 layer, indicating that the $CrI_3/NiCl_2$ vdW heterostructure in this region of the electric field displays unique type-I band alignments.

However, in the range $[-0.1, 0.8]$ V/Å of the external electric field, the CBM is composed of spin-down bands, while the VBM is composed of spin-up bands as illustrated in Fig. 4(b), indicating that the vdW heterostructure can be easily converted to BMSs in this region [69–72,76]. Meanwhile, the VBM is located at the Γ point, while the CBM lies in the Γ-M line and is close to the M point, as illustrated in Fig. 3, suggesting that in this region the $CrI_3/NiCl_2$ vdW heterostructure is an indirect-band-gap semiconductor. Moreover, in this range of electric field, the CBM is contributed mainly by the CrI_3 layer, while the VBM is contributed mainly by the $NiCl_2$ layer, confirming further that the $CrI_3/NiCl_2$ vdW heterostructure hosts unique type-II band alignments. Therefore, the FM semiconducting features can occur easily in every layer of the $CrI_3/NiCl_2$ vdW heterostructure.

C. Nearly perfect SSE and SFE in the $CrI_3/NiCl_2$ vdW heterostructure

From the above discussions, one can find that one of the key conditions, i.e., the FM semiconducting feature to realize the SSE, occurs in the every layer of the $CrI_3/NiCl_2$ vdW heterostructure. In Fig. 5(a), we designed the related spin caloritronic device, which consisted of three parts, i.e.,

the left (right) lead with temperature T_L (T_R) and the central scattering region. As a temperature gradient ΔT ($=T_L - T_R$) is produced, the spin-dependent currents (I_σ) are generated, and they can be calculated in the Landauer-Büttiker formula [77],

$$I_\sigma = \frac{e}{h} \int_{-\infty}^{+\infty} \{T_\sigma(E)[f_L(E, T_L) - f_R(E, T_R)]\} dE, \quad (1)$$

where σ stands for spin-up or spin-down, e is the electronic charge, h is the Planck constant, and the equilibrium Fermi-Dirac distribution of the left (right) lead at temperature $T_{L(R)}$ is given by the equation $f_{L(R)}(E, T_{L(R)}) = \{1 + \exp[(E - \mu_{L(R)})/k_B T_{L(R)}]\}^{-1}$. $\mu_{L(R)}$ is the chemical potential for the left (right) lead. The spin-resolved transmission coefficients of the device can be calculated by using the NEGF in the linear-resonance regime [78–82] as $T_\sigma(E) = \text{Tr}[\Gamma_L G^R(E)\Gamma_R G^A(E)]$, where $\Gamma_{L/R} = i|\Sigma_{L/R} - \Sigma_{L/R}^\dagger|$ indicates the interaction between the central scattering region and the left (right) lead, whose self-energy is $\Sigma_{L/R}$. $G^{R/A}(E)$ represents the retarded (advanced) Green's function of the central scattering region, $\Gamma_{L/R} = [H_c - (E + i\eta) + \Sigma_L + \Sigma_R]^{-1}$, and $G^A(E) = [G^R(E)]^\dagger$, where H_c is the Hamiltonian in the central scattering region. Note that the temperature gradient between two leads is adopted as small values with $|\Delta T| \ll T_{L(R)}$, and the system produces a remarkably small potential difference $\Delta \mu \ll \mu_{L(R)}$.

In Fig. 5(b), the thermally driven spin-up current I_{up} and spin-down current I_{dn} transported through the CrI$_3$/NiCl$_2$ vdW heterostructure are plotted as a function of T_L. One can see that $I_{up} < 0$ while $I_{dn} > 0$ characterized by the same threshold temperature T_h, indicating that the thermal spin-up and spin-down currents flow just in the positive directions. This spin-dependent transport behavior is a typical feature of the conduction electron-based SSE. Moreover, the curves of I_{up} are nearly symmetrical with those of I_{dn} about the zero-current axis, indicating that a nearly pure thermal spin current without any accumulation of charge currents can be achieved in the device [14,83,84], which supports further the occurrence of a well-defined SSE in the CrI$_3$/NiCl$_2$ vdW heterostructure.

To elucidate the underlying physical mechanism of the SSE appearing here, we fall back on the Landauer-Büttiker formula described above. One can see that the spin-dependent currents depend mainly on the transmission coefficients and the difference of Fermi-Dirac distributions between two leads. Considering the fact that the difference of Fermi-Dirac distributions of the two leads is induced by their different temperatures ($T_L > T_R$), two kinds of carrier transport may occur: (i) the carriers with energy higher than the Fermi level flow from the hot lead to the cold, producing the electron current (I_e), and (ii) the carriers with energy lower than the Fermi level flow from the cold lead to the hot, leading to the hole current (I_h). As the transmission spectrum is independent of energy, I_e and I_h will cancel each other, leading to a net thermal carrier current. It is interesting that the transmission spectrum of the CrI$_3$/NiCl$_2$ vdW heterostructure is spin splitting with a finite band gap, as illustrated in Fig. 5(c), where a spin-up transmission peak is located above the Fermi level, while a spin-down transmission peak is located below the Fermi level nearly symmetrically, breaking

the electron-hole symmetry of the system. As a consequence, the spin-dependent currents are produced, and as a temperature gradient is adopted, the spin-up current is driven to flow from the left lead to the right, while the spin-down current flows in the opposite direction [14,83,84].

Furthermore, by examining the atomic orbital contributions to the spin-dependent transmission channels near the Fermi levels from the transmission spectra [see Fig. 5(c)] and the corresponding band structures [see Fig. 2(a)], one can conclude that the spin-up transport channel above the Fermi level is contributed by the Ni atoms in the NiCl$_2$ layer, while the spin-down transport channel below the Fermi level is contributed by the Cr atoms in the CrI$_3$ layer. This property indicates that the spin-up and spin-down currents flow in different layers, i.e., the spin-up current transports in the NiCl$_2$ layer while the spin-down current transports in the CrI$_3$ layer, as illustrated in Fig. 5(a). These unique transport features support the idea that a nearly perfect SFE with the spin polarization as high as 100% occurs in every layer of the CrI$_3$/NiCl$_2$ vdW heterostructure, and that the thermal spin-up and spin-down currents can be manipulated independently toward particular device applications.

IV. CONCLUSION

In summary, we constructed a typical CrI$_3$/NiCl$_2$ vdW heterostructure, and we investigated its magnetic configurations and thermally driven spin currents systematically by using the first-principles calculations combined with the NEGF method. The theoretical results show that the CrI$_3$/NiCl$_2$ vdW heterostructure displays a stable stacking configuration, and its magnetic state can be manipulated and adjusted by an external electric field. In the range [−0.8, −0.2] V/Å of the electric field, the vdW heterostructure has a FM ground state, while in the range [−0.1, 0.8] V/Å it is converted to an AFM semiconductor. Moreover, as the electric field is increased to the range [−0.1, 0.8] V/Å, the CrI$_3$/NiCl$_2$ vdW heterostructure is changed to an indirect-band-gap BMS characterized by a type-II band alignment, while in the range [−0.8, −0.2] V/Å it becomes a direct-band-gap magnetic semiconductor. These rich magnetic configurations, especially the FM semiconducting properties in every layer of the vdW heterostructure, support its potential spintronic device applications. Furthermore, we proposed a spin caloritronic device based on the CrI$_3$/NiCl$_2$ vdW heterostructure, and we found that a well-defined SSE occurs and a nearly pure thermal spin current can be generated. In addition, every layer of the vdW heterostructure displays a nearly perfect SFE with the spin polarization as high as 100%. Our theoretical results propose a class of structural candidates to realize spin caloritronic devices characterized by multiple inspiring thermal-spin effects.

Note added. The numerical results of Model A of the CrI$_3$/NiCl$_2$ vdW heterostructure without Coulomb correlation both in Ni and Cr atoms are presented in Sec. II of the Supplemental Material [52], and the numerical results of Model B without and with **U** are provided, respectively, in Secs. III and IV of the Supplemental Material [52], which show very similar numerical results, supporting the robustness of the spin caloritronic device design of the current vdW heterostructure. Moreover, in a recent experimental work

[85], some spin caloritronic effects have been observed successfully in a $CrBr_3$-based magnetic vdW heterostructure, supporting the idea that the vdW heterostructures and the related thermal-spin effects proposed here can be realized in experiments.

[1] K. Uchida, S. Takahashi, K. Harii, J. Ieda, W. Koshibae, K. Ando, S. Maekawa, and E. Saitoh, Nature (London) **455**, 778 (2008).

[2] M. Zeng, Y. Feng, and G. Liang, Nano Lett. **11**, 1369 (2011).

[3] G. E. W. Bauer, E. Saitoh, and B. J. Van Wees, Nat. Mater. **11**, 391 (2012).

[4] S. T. Goennenwein and G. E. Bauer, Nat. Nanotech. **7**, 145 (2012).

[5] S. R. Boona, R. C. Myers, and J. P. Heremans, Energ. Environ. Sci. **7**, 885 (2014).

[6] H. O. Frota and A. Ghosh, Solid State Commun. **191**, 30 (2014).

[7] J. F. Sierra, I. Neumann, J. Cuppens, B. Raes, M. V. Costache, and S. O. Valenzuela, Nat. Nanotech. **13**, 107 (2018).

[8] L. Gu, H.-H. Fu, and R. Wu, Phys. Rev. B **94**, 115433 (2016).

[9] L. Yi, D. Yang, M. Liu, H.-H. Fu, L. Ding, Y. Xu, B. Zhang, L. Pan, and J. Q. Xiao, Adv. Funct. Mater. **30**, 2004024 (2020).

[10] C. M. Jaworski, J. Yang, S. Mack, D. D. Awschalom, J. P. Heremans, and R. C. Myers, Nat. Mater. **9**, 898 (2010).

[11] K.-I. Uchida, H. Adachi, T. Ota, H. Nakayama, S. Maekawa, and E. Saitoh, Appl. Phys. Lett. **97**, 172505 (2010).

[12] S. M. Wu, W. Zhang, Amit KC, P. Borisov, J. E. Pearson, J. S. Jiang, D. Lederman, A. Hoffmann, and A. Bhattacharya, Phys. Rev. Lett. **116**, 097204 (2016).

[13] K.-I. Uchida, J. Xiao, H. Adachi, J.-I. Ohe, S. Takahashi, J. Ieda, T. Ota, Y. Kajiwara, H. Umezawa, H. Kawai *et al.*, Nat. Mater. **9**, 894 (2010).

[14] H.-H. Fu, G.-F. Du, D.-D. Wu, Q.-B. Liu, and R. Wu, Phys. Rev. B **100**, 085407 (2019).

[15] Q.-B. Liu, D.-D. Wu, and H.-H. Fu, Phys. Chem. Chem. Phys. **19**, 27132 (2017).

[16] B. Z. Rameshti and A. G. Moghaddam, Phys. Rev. B **91**, 155407 (2015).

[17] B. Zhou, B. Zhou, Y. Zeng, G. Zhou, and T. Ouyang, J. Appl. Phys. **117**, 104305 (2015).

[18] H.-H. Fu, L. Gu, and D.-D. Wu, Phys. Chem. Chem. Phys. **18**, 12742 (2016).

[19] Y. S. Liu, X. Zhang, X. F. Yang, X. K. Hong, J. F. Feng, M. S. Si, and X. F. Wang, Phys. Chem. Chem. Phys. **17**, 10462 (2015).

[20] H.-H. Fu, D.-D. Wu, L. Gu, M. Wu, and R. Wu, Phys. Rev. B **92**, 045418 (2015).

[21] J. Li, B. Wang, F. Xu, Y. Wei, and J. Wang, Phys. Rev. B **93**, 195426 (2016).

[22] M. Wierzbowska and A. Dominiak, Carbon **80**, 255 (2014).

[23] X.-Y. Tan, D.-D. Wu, Q.-B. Liu, H.-H. Fu, and R. Wu, J. Phys.: Condens. Matter **30**, 355303 (2018).

[24] D.-D. Wu, H.-H. Fu, Q.-B. Liu, and R. Wu, J. Mater. Chem. C **6**, 10603 (2018).

[25] A. K. Geim and I. V. Grigorieva, Nature (London) **499**, 419 (2013).

[26] C. R. Dean, A. F. Young, I. Meric, C. Lee, L. Wang, S. Sorgenfrei, K. Watanabe, T. Taniguchi, P. Kim, K. L. Shepard, and J. Hone, Nat. Nanotech. **5**, 722 (2010).

[27] D. Jariwala, T. J. Marks, and M. C. Hersam, Nat. Mater. **16**, 170 (2017).

[28] Y. Liu, N. O. Weiss, X. Duan, H.-C. Cheng, Y. Huang, and X. Duan, Nat. Rev. Mater. **1**, 16042 (2016).

[29] K. S. Novoselov, A. Mishchenko, A. Carvalho, and A. H. C. Neto, Science **353**, aac9439 (2016).

[30] R. Xiang, T. Inoue, Y. Zheng, A. Kumamoto, Y. Qian, Y. Sato, M. Liu, D. Tang, D. Gokhale, J. Guo, K. Hisama, S. Yotsumoto, T. Ogamoto, H. Arai, Y. Kobayashi, H. Zhang, B. Hou, A. Anisimov, M. Maruyama, Y. Miyata, S. Okada, S. Chiashi, Y. Li, J. Kong, E. I. Kauppinen, Y. Ikuhara, K. Suenaga, and S. Maruyama, Science **367**, 537 (2020).

[31] N. Mounet, M. Gibertini, P. Schwaller, D. Campi, A. Merkys, A. Marrazzo, T. Sohier, I. E. Castelli, A. Cepellotti, G. Pizzi, and N. Marzari, Nat. Nanotech. **13**, 246 (2018).

[32] D. Torelli, K. S. Thygesen, and T. Olsen, 2D Mater. **6**, 045018 (2019).

[33] M. Gibertini, M. Koperski, A. F. Morpurgo, and K. S. Novoselov, Nat. Nanotech. **14**, 408 (2019).

[34] H. Liu, J.-T. Sun, M. Liu, and S. Meng, J. Phys. Chem. Lett. **9**, 6709 (2018).

[35] W. Xiong, C. Xia, J. Du, T. Wang, X. Zhao, Y. Peng, Z. Wei, and J. Li, Phys. Rev. B **95**, 245408 (2017).

[36] J. Du, C. Xia, W. Xiong, T. Wang, Y. Jia, and J. Li, Nanoscale **9**, 17585 (2017).

[37] A. ToolKit, http://www.quantumwise.com (2014).

[38] M. Brandbyge, J.-L. Mozos, P. Ordejón, J. Taylor, and K. Stokbro, Phys. Rev. B **65**, 165401 (2002).

[39] J. P. Perdew and Y. Wang, Phys. Rev. B **45**, 13244 (1992).

[40] J. P. Perdew, K. Burke, and M. Ernzerhof, Phys. Rev. Lett. **77**, 3865 (1996).

[41] S. Grimme, S. Ehrlich, and L. Goerigk, J. Comput. Chem. **32**, 1456 (2011).

[42] N. Troullier and J. L. Martins, Phys. Rev. B **43**, 1993 (1991).

[43] S. L. Dudarev, G. A. Botton, S. Y. Savrasov, C. J. Humphreys, and A. P. Sutton, Phys. Rev. B **57**, 1505 (1998).

[44] J. Y. Liu, Q. Sun, K. Y., and P. Jena, Phys. Chem. Chem. Phys. **18**, 8777 (2016).

[45] F. Subhan and J. Hong, J. Phys. Chem. C **124**, 7156 (2020).

[46] J. Xiao and B. Yan, 2D Mater. **7**, 045010 (2020).

[47] M. A. McGuire, H. Dixit, V. R. Cooper, and B. C. Sales, Chem. Mater. **27**, 612 (2015).

[48] N. Richter, D. Weber, F. Martin, N. Singh, U. Schwingenschlögl, B. V. Lotsch, and M. Kläui, Phys. Rev. Mater. **2**, 024004 (2018).

[49] R. W. Wyckoff, *Crystal Structures* (Interscience Publishers, New York, 1963), Vol. 1, p. 239.

[50] L. Webster and J. A. Yan, Phys. Rev. B **98**, 144411 (2018).

[51] M. Lu, Q. Yao, C. Xiao, C. Huang, and E. Kan, ACS Omega **4**, 5714 (2019).

[52] See Supplemental Material at http://link.aps.org/supplemental/10.1103/PhysRevB.103.115415 for electronic structures of the

CrI$_3$ and NiCl$_2$ monolayers with and without considering Coulomb correlation **U** and others.

[53] Y.-H. Lee, X.-Q. Zhang, W. Zhang, M.-T. Chang, C.-T. Lin, K.-D. Chang, Y.-C. Yu, J. T.-W. Wang, C.-S. Chang, L.-J. Li, and T.-W. Lin, Adv. Mater. **24**, 2320 (2012).

[54] K.-K. Liu, W. J. Zhang, Y.-H. Lee, Y.-C. Lin, M.-T. Chang, C.-Y. Su, C.-S. Chang, H. Li, Y. Shi, H. Zhang *et al.*, Nano Lett. **12**, 1538 (2012).

[55] Y. Zhan, Z. Liu, S. Najmaei, P. M. Ajayan, and J. Lou, Small **8**, 966 (2012).

[56] Q. Liu, X. Li, Q. He, A. Khalil, D. Liu, T. Xiang, X. Wu, and L. Song, Small **11**, 5556 (2015).

[57] M. Acerce, D. Voiry, and M. Chhowalla, Nat. Nanotech. **10**, 313 (2015).

[58] J. Yang, K. Wang, J. Zhu, C. Zhang, and T. Liu, ACS Appl. Mater. Interfaces **8**, 31702 (2016).

[59] S. J. R. Tan, S. Sarkar, X. Zhao, X. Luo, Y. Z. Luo, S. M. Poh, I. Abdelwahab, W. Zhou, T. Venkatesan, W. Chen, S. Y. Quek, and K. P. Loh, ACS Nano **12**, 5051 (2018).

[60] K. Chang, X. Hai, H. Pang, H. Zhang, L. Shi, G. Liu, H. Liu, G. Zhao, M. Li, and J. Ye, Adv. Mater. **28**, 10033 (2016).

[61] Y. Feng, X. Wu, J. Han, and G. Gao, J. Mater. Chem. C **6**, 4087 (2018).

[62] P. Jiang, C. Wang, D. Chen, Z. Zhong, Z. Yuan, Z.-Y. Lu, and W. Ji, Phys. Rev. B **99**, 144401 (2019).

[63] C. Wang, X. Zhou, Y. Pan, J. Qiao, X. Kong, C.-C. Kaun, and W. Ji, Phys. Rev. B **97**, 245409 (2018).

[64] W. Y. Kim and K. S. Kim, Nat. Nanotech. **3**, 408 (2008).

[65] Y.-W. Son, M. L. Cohen, and S. G. Louie, Nature (London) **444**, 347 (2006).

[66] M. Wu, X. Wu, Y. Gao, and X. C. Zeng, Appl. Phys. Lett. **94**, 223111 (2009).

[67] N. Han, D. Yang, C. Zhang, X. Zhang, J. Shao, Y. Cheng, and W. Huang, J. Phys. Chem. Lett. **11**, 9453 (2020).

[68] In the type-I (-II) vdW heterostructures, the CB maximum and the VB minimum in their energy bands are contributed by the atoms in the different (same) layers.

[69] X. Li, X. Wu, Z. Li, J. Yang, and J. G. Hou, Nanoscale **4**, 5680 (2012).

[70] V. V. Bannikov and A. L. Ivanovskii, JETP Lett. **96**, 735 (2013).

[71] L. Yuan, Z. Li, and J. Yang, Phys. Chem. Chem. Phys. **15**, 497 (2013).

[72] J. Zhang, X. Li, and J. Yang, Appl. Phys. Lett. **104**, 172403 (2014).

[73] X. Li and J. Yang, Nat. Sci. Rev. **3**, 365 (2016).

[74] B. Huang, G. Clark, E. Navarro-Moratalla, D. R. Klein, R. Cheng, K. L. Seyler, D. Zhong, E. Schmidgall, M. A. McGuire, D. H. Cobden *et al.*, Nature (London) **546**, 270 (2017).

[75] Z. Wang, T. Zhang, M. Ding, B. Dong, Y. Li, M. Chen, X. Li, J. Huang, H. Wang, X. Zhao, Y. Li, D. Li, C. Jia, L. Sun, H. Guo, Y. Ye, D. Sun, Y. Chen, T. Yang, J. Zhang, S. Ono, Z. Han, and Z. Zhang, Nat. Nanotech. **13**, 554 (2018).

[76] X. Tan, L. Liu, H. Xiang, G.-F. Du, A. Lou, and H.-H. Fu, Nanoscale **12**, 8942 (2020).

[77] Y. Imry and R. Landauer, Rev. Mod. Phys. **71**, S306 (1999).

[78] H.-H. Fu, K.-L. Yao, and Z.-L. Liu, J. Chem. Phys. **128**, 114705 (2008).

[79] H.-H. Fu, K.-L. Yao, and Z.-L. Liu, J. Phys. Chem. A **112**, 6205 (2008).

[80] H.-H. Fu and K.-L. Yao, J. Chem. Phys. **134**, 054903 (2011).

[81] H.-H. Fu, K.-L. Yao, and Z.-L. Liu, J. Chem. Phys. **129**, 134706 (2008).

[82] H.-H. Fu and K.-L. Yao, J. Appl. Phys. **111**, 124510 (2012).

[83] D.-D. Wu, H.-H. Fu, Q.-B. Liu, G.-F. Du, and R. Wu, Phys. Rev. B **98**, 115422 (2018).

[84] D.-D. Wu, G.-F. Du, and H.-H. Fu, J. Mater. Chem. C **8**, 4486 (2020).

[85] T. Liu, J. Peiro, D. K. de Wal, J. C. Leutenantsmeyer, M. H. D. Guimaraes, and B. J. van Wees, Phys. Rev. B **101**, 205407 (2020).